


 Cite this: *Lab Chip*, 2015, 15, 3326

## A microfluidics approach to study the accumulation of molecules at basal lamina interfaces†

 Fabienna Arends,<sup>ab</sup> Sabine Sellner,<sup>c</sup> Philipp Seifert,<sup>d</sup> Ulrich Gerland,<sup>d</sup> Markus Rehberg<sup>c</sup> and Oliver Lieleg<sup>\*ab</sup>

For an efficient distribution of drugs and drug carriers through biological barriers such as the vascular system, the size and surface properties of nanoparticles and molecules play a key role. To screen for important parameters which determine the ability of drugs or drug carriers to translocate through complex biological barriers, an *in vitro* assay which correctly predicts the behavior of those objects *in vivo* would be highly desirable. Here, we present a microfluidic setup to probe the diffusive spreading of molecules with different net charges and molecular weights through a basal lamina interface – a biopolymer system which contributes to the barrier function of the vascular system and the skin. From our data, we find a charge dependent accumulation of molecules at the gel interface which is consistent with transient binding of those molecules to the gel constituents. We also observe a similar charge-dependent accumulation of molecules in living mice where the test molecules colocalize with collagen IV, a key component of the basal lamina. Our assay may serve as a platform to perform penetration experiments with even more complex interfaces combining cellular barriers with biopolymer coatings.

 Received 19th May 2015,  
Accepted 2nd July 2015

DOI: 10.1039/c5lc00561b

[www.rsc.org/loc](http://www.rsc.org/loc)

### Introduction

In the human body, complex biological barriers prevent the entrance and distribution of pathogens and other foreign compounds. In addition to their protective function, these barriers also regulate the passage of beneficial molecules such as nutrients, growth factors, proteins, hormones or polysaccharides.<sup>1–3</sup> Examples for such complex biological barriers in the human body include the blood–brain-barrier,<sup>4</sup> the skin,<sup>5</sup> the gastrointestinal tract,<sup>6</sup> the oral cavity<sup>7</sup> and the vascular system.<sup>8</sup> All these examples share a common structure: they consist either of endothelial cells (blood–brain barrier and vascular system) or epithelial cells (oral cavity, skin and gastrointestinal tract) which are coated by a biopolymer matrix. This extracellular matrix (ECM) can be located on the outer side of the cell layer where it constitutes the first line of

defense against pathogens as in the oral cavity or the gastrointestinal tract.<sup>9</sup> Alternatively, the ECM may also be located on the basolateral side of the cell layer as it is the case for the basal lamina surrounding blood vessels. Here, the passage of molecules and cells from the blood stream into the adjoining tissue is primarily regulated by the endothelial cells. However, compared to physiologic conditions, the ECM layer becomes more accessible for molecules when the endothelium becomes leaky *e.g.* during inflammation, infection, or in the presence of a tumor.<sup>10,11</sup> Moreover, macromolecules which are bi-directionally exchanged between the blood stream and the interstitium by transcytosis, a mechanism particularly prominent in vascular endothelial cells,<sup>12</sup> need to pass the basal lamina. Similarly, if molecules from the connective tissue are supposed to enter into the blood stream, *e.g.* in the case of subcutaneous injection of heparin or insulin, they need to cross the basal lamina from the basolateral side of the blood vessel wall. In those cases, the basal lamina acts as the primary barrier.

Advanced drug delivery methods make use of the leaky endothelium for the specific targeting of tumors.<sup>13</sup> The efficiency of drug carriers to pass the endothelium and the ECM barrier can depend on several parameters *e.g.* particle size, shape and surface modification. Experiments conducted in bulk systems showed that ECM gels show a high selectivity for nanoparticles based on their charge and hydrophobicity.<sup>14,15</sup> However, the diffusive entry of particles into the ECM

<sup>a</sup> Institute of Medical Engineering IMETUM, Technische Universität München, Boltzmannstrasse 11, 85748 Garching, Germany. E-mail: [oliver.lieleg@TUM.de](mailto:oliver.lieleg@TUM.de)

<sup>b</sup> Department of Mechanical Engineering, Technische Universität München, Boltzmannstrasse 15, 85748 Garching, Germany

<sup>c</sup> Walter Brendel Centre of Experimental Medicine, Ludwig-Maximilians-Universität München, Marchioninistr. 15, 81377 Munich, Germany

<sup>d</sup> Department of Physics, Technische Universität München, James-Frank-Str.1, 85748 Garching, Germany

† Electronic supplementary information (ESI) available. See DOI: 10.1039/c5lc00561b



at the interface between the basal lamina and a liquid phase (such as the blood stream) cannot be characterized in those bulk experiments. In addition to the diffusion behavior of nanoparticles also the spreading of encapsulated drug molecules, once they are released, is of great interest.<sup>16</sup> To investigate both, two approaches are possible: *in vivo* experiments in mammals such as mice, rats, rabbits or *in vitro* testing in an appropriate tissue-on-a-chip setup. A pre-screening for important parameters in a robust *in vitro* setup which reliably predicts the diffusive spreading of pharmaceuticals *in vivo* would be highly desirable since it would reduce the need of animal tests.<sup>17</sup>

One promising approach for the realization of such predictive *in vitro* experiments is microfluidics.<sup>18,19</sup> There are already a broad range of experimental settings in which such an approach is used, e.g. for the design of a cardiac tissue model,<sup>20</sup> for the investigation of nanoparticle translocation across a permeable endothelium<sup>21</sup> or through a endothelial/epithelial double layer simulating the biological interface in alveoli.<sup>22</sup> Those chips are able to reproduce key results obtained in living tissue in an *in vitro* setting although their setup is strongly simplified: to date, most of those microfluidic penetration assays mainly focus on the barrier function of the cell layer and neglect the influence of the adjacent biopolymer matrix. This is partly due to the fact that it is technically challenging to deposit a soft biopolymer gel on a microfluidics chip in such a way that a stable gel/liquid interface is generated which can be used for a penetration experiment. First realizations of such a molecular penetration experiment with a biopolymer gel have been achieved for mucin gels,<sup>23,24</sup> but are still lacking for other gels such as the basal lamina.

Here, we present a microfluidic assay for the quantification of the diffusive transport of molecules across basal lamina interfaces. As a model system for the basal lamina, we use an extracellular matrix gel which has been purified from the Engelbreth–Holm–Swarm sarcoma of mice. We compare the penetration efficiency of different fluorescent molecules

such as dextrans with different molecular weights and net charges as well as customized peptides. In our microfluidics setup, those molecules accumulate at the gel/buffer interface in a charge selective manner in full agreement with model calculations considering transient binding of molecules to the gel components. *In vivo* microinjection experiments conducted in mice show a similar charge selective accumulation of those molecules around blood vessels and a colocalization with collagen IV, a key component of the basal lamina. Thus, our *in vitro* setup successfully predicts the selective transport of molecules across this biological barrier.

## Results and discussion

### Generating a stable gel/liquid interface on chip

To study the diffusion of different solutes across an extracellular matrix gel we first design a microfluidic chip which allows us to generate a stable gel/liquid interface. As shown in Fig. 1 (for more details see Fig. S1†), this chip has one outlet and two inlets, one for inserting the ECM and one for inserting buffer with fluorescent solutes. Liquid (*i.e.* ice-cold) ECM is filled into the chip through inlet 1. Here, at half the channel length, a “finger-like” structure begins where five pillars divide the main channel into six smaller channels of identical width.

When liquid ECM is filled into inlet 1, it can be carefully pushed into this finger-like structure until, at the end of the pillars, surface tension effects ensure stopping of the liquid (see inset of Fig. 1) and prevent it from entering into the buffer channel which is oriented perpendicular to the pillars. With this setup, a well-defined liquid/air interface is created which is important for the following experiments. As the ECM is inserted into the chip in its liquid state, gelation has to be induced on chip. Such a gelation of ECM is usually achieved by a heating step to 37 °C for 30 minutes (see Methods). However, we here induce gelation at room temperature since all following experiments are conducted at this temperature. During gel formation, it is important to prevent

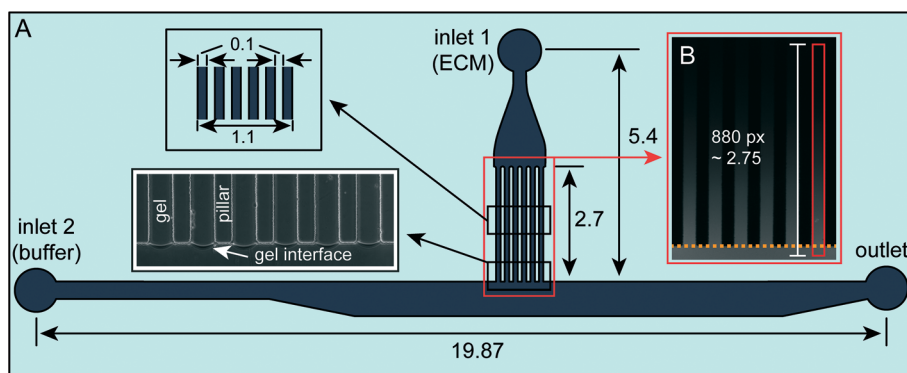


**Fig. 1** (A) The microfluidic chip has two inlets: inlet 1 for inserting the ECM and inlet 2 for inserting buffer together with fluorescent molecules of interest. The pillar structure prevents the injected ECM from entering the lower channel due to surface tension. (B) For data analysis, the fluorescence intensity within each channel is measured within a rectangular area with a length of 880 pixels corresponding to 2.75 mm. The lower end of the rectangle is placed 50 pixels into the lower channel so that the bulk intensity in the buffer channel is obtained as well. The orange dotted line denotes the position of the gel/buffer interface. All dimensions in the shown scheme are given in mm.



drying of the ECM – especially at the interface to the compartment which will be filled with fluorescent solutes. A naive approach to avoid such drying of the ECM interface might be to induce gel formation at a water interface. This could be achieved by inserting an aqueous solution, *e.g.* buffer, through inlet 2 directly after loading the chip with the liquid ECM. However, as gelation requires some time, the mechanical strength of the ECM is still weak when the buffer is inserted, and thus the integrity of the ECM compartment is disturbed by buffer influx. Furthermore, when placed at an aqueous interface during gelation, the ECM tends to swell and locally dissolves which in turn results in a diffuse gel interface. A better solution would be to perform gelation at an interface with a hydrophobic fluid that is immiscible with the ECM (and thus does not dissolve the ECM matrix) but still prevents drying. We chose a polydimethylsiloxane oil (PDMS) which fulfills those requirements and is based on the same polymer used for crafting the microfluidic chip. We insert the PDMS oil through inlet 2 into the lower channel and keep it in this compartment until ECM gelation is finished. The oil is then removed from the chip through the outlet and replaced by PBS buffer which is inserted through inlet 2. When the PBS is inserted into the channel, a clear interface between PBS and PDMS oil is visible under the microscope. This feature allowed us to monitor the proper removal of the oil from the channel. With this approach, we are able to generate intact gel/buffer interfaces with which we obtain reproducible penetration profiles with different test molecules.

### DEAE-dextrans accumulate at the ECM/buffer interface

We first investigate the correlation between the diffusion efficiency of molecules across an ECM interface and their net charge. We use two variants of FITC-labeled dextrans with a molecular weight of 150 kDa, and those dextrans carry a certain percentage of either diethylaminoethyl (DEAE) or carboxymethyl groups (CM). For the experiments, both sorts of dextrans are dissolved in PBS at a concentration of 10 mg mL<sup>-1</sup>. Since the pH of the solution is neutral, the DEAE groups are protonated and therefore positively charged, whereas the CM groups are deprotonated and thus negatively

charged (see also Table 1). The PBS-dextran solution is inserted into the microfluidic chip through inlet 2 and the results of the experiment 60 min after dextran insertion are shown in Fig. 2: negatively charged CM-dextrans (Fig. 2A) enter the gel without showing noticeable accumulation at the ECM/buffer interface whereas DEAE-dextrans do accumulate (Fig. 2B, white arrows). This difference is somewhat astonishing as previous experiments have demonstrated that both negatively and positively charged objects can be trapped in ECM gels.<sup>14,15,25</sup> However, it is important to recall that ECM gels immobilize positively charged particles more efficiently than negatively charged ones – a behavior which was suggested to arise from the high concentration of negatively charged heparan sulfate in ECM gels.<sup>14</sup> The higher tolerance of the ECM gel for negatively charged nanoparticles could also explain why DEAE-dextrans, which have a net charge of +200e, and CM-dextrans with a net charge of -165e show a different behavior at the gel/buffer interface.

In the bulk volume of the ECM gel, the intensity profiles obtained for the two 150 kDa dextran variants are very similar (Fig. 2C, solid lines and Fig. S2†) and suggest diffusive spreading of those molecules throughout the ECM. Transient binding events as reported for polystyrene particles<sup>15</sup> and growth factors<sup>26</sup> in ECM gels might also occur between the dextran molecules and the ECM components within the bulk volume of the gel, but are likely to take place on the time scale of seconds or below. Thus, on the time scales studied here, these transient binding events of single molecules might give rise to a bulk transport that resembles that of a freely diffusing particle ensemble. Considering that dextrans, which have a hydrodynamic radius of a few nm,<sup>27</sup> are several orders of magnitude smaller than the mesh size of the ECM gel (which is in the μm range<sup>14</sup>), molecule-polymer interactions will be rare both in the bulk volume of the ECM as well as at the ECM/buffer interface. However, we speculate that the high concentration of dextran molecules in the buffer compartment balances the rareness of the binding events giving rise to the observed accumulation of molecules at the gel/liquid interface. To test this hypothesis, we model the diffusive entry of molecules into a gel compartment. For this model, we make the following assumptions: in the buffer compartment the DEAE-dextrans are present at high concentrations and diffuse freely. However, as soon as they reach the buffer/ECM interface they can transiently bind to the ECM network which temporarily interrupts their diffusive penetration of the gel (see Methods and ESI† for details). The results obtained for such calculated penetration profiles are shown in Fig. 3A. Indeed, our simple model returns a penetration profile with a clear accumulation peak at the liquid/gel interface. However, in the bulk volume of the gel phase, the calculated penetration profiles are largely independent from whether or not transient binding events to the gel matrix are considered. This is in agreement with the results from our *in vitro* experiments where we obtained similar penetration profiles for DEAE- and CM-dextrans in the bulk part of the gel.

**Table 1** Properties of dextrans and peptides used in the study. The molecular weight was given by the supplier and the charge was calculated assuming that all carboxyl- and amine-groups are charged

Name	Molecular weight [kDa]	Fluorophore type, fluorophore charge [e]	Maximum charge [e]
CM-dextran	150	FITC, -1	-165
DEAE-dextran	150	FITC, -1	+200
CM-dextran	4	FITC, -1	-4
DEAE-dextran	4	FITC, -1	+5
(KKK) <sub>8</sub>	4	TAMRA, 0	+23
(QQK) <sub>8</sub>	4	TAMRA, 0	+7
(EEE) <sub>8</sub>	4	TAMRA, 0	-25
(QQE) <sub>8</sub>	4	TAMRA, 0	-9



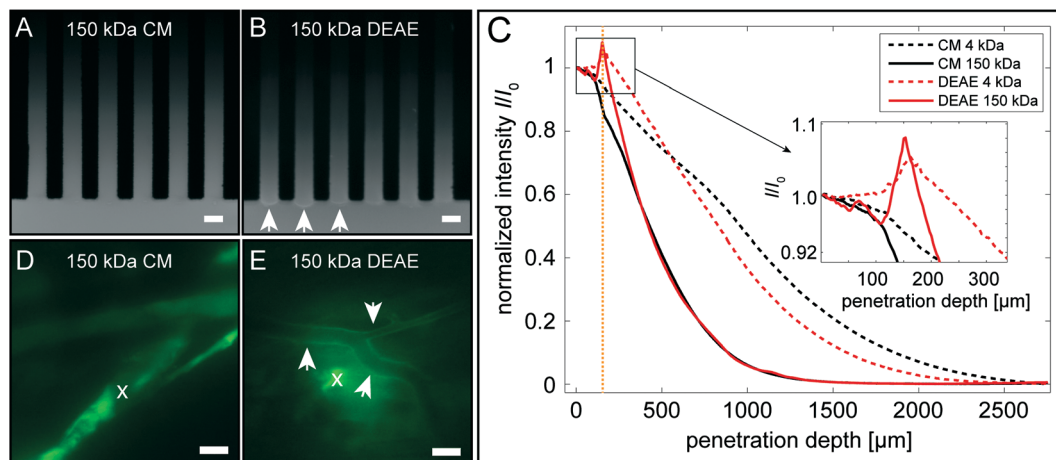


**Fig. 2** Fluorescence images of negatively charged CM- (A) and positively charged DEAE-dextrans (B) ( $MW = 150$  kDa) *in vitro* 60 min after their insertion into the chip. The white arrows point at accumulation sites of DEAE-dextran at the buffer/gel interface. The scale bar denotes  $100 \mu\text{m}$ . (C) The corresponding intensity profiles are plotted for positively and negatively charged dextrans of two different molecular weights each. The orange dotted line marks the gel-buffer interface. (D) and (E) show representative images of the spatial distribution of dextrans 60 min after they have been microinjected into the cremaster muscle of a mouse. The CM-dextrans rapidly spread from the injection site (white cross) next to muscle fibers (D) whereas DEAE-dextrans accumulate around blood vessels (white arrows) (E). Scale bar:  $50 \mu\text{m}$ .

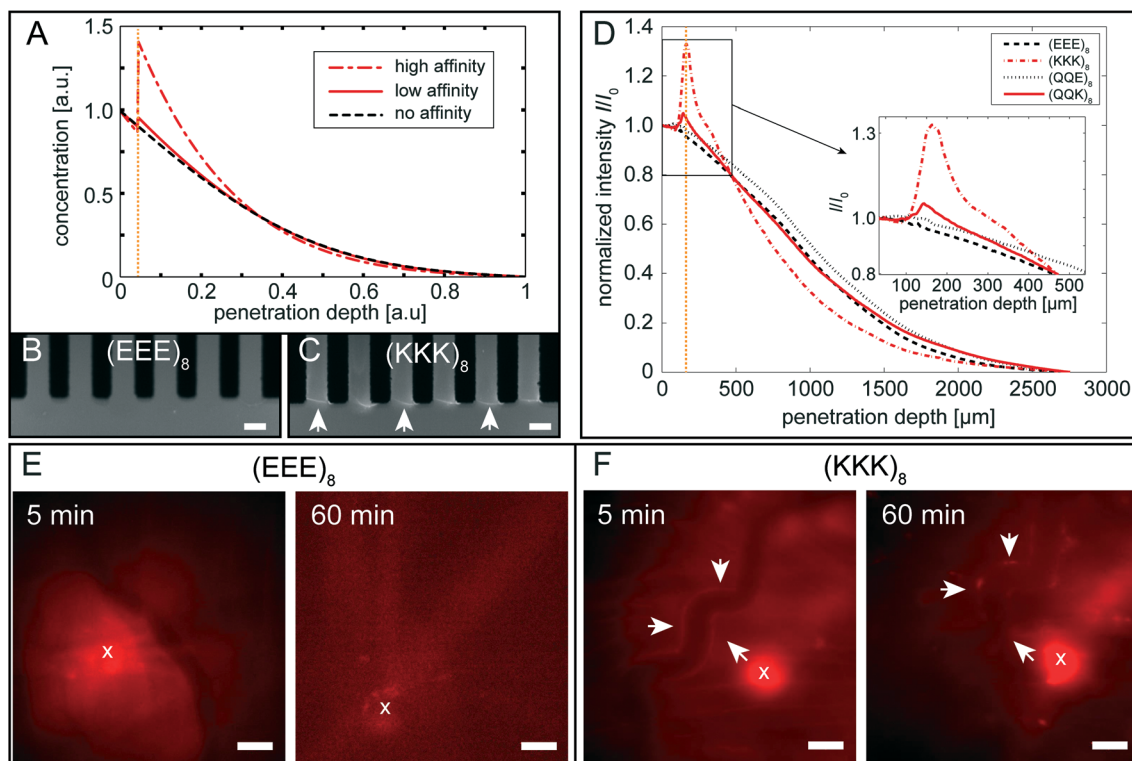


**Fig. 3** Molecular penetration profiles are calculated from a model that assumes transient binding of diffusing molecules to the gel components (A). If this binding affinity is set to zero, normal diffusive spreading is obtained. Conversely, the model predicts an accumulation peak at the buffer/gel interface with the height of this peak depending on the strength of the binding affinity. Fluorescence images of negatively  $(\text{EEE})_8$  (B) and positively charged  $(\text{KKK})_8$  (C) peptides *in vitro* 60 min after buffer insertion are consistent with the model prediction. The white arrows indicate accumulation of peptides at the interface. The scale bar denotes  $100 \mu\text{m}$ . (D) The corresponding intensity profiles are plotted for negatively charged  $(\text{EEE})_8$  and  $(\text{QQE})_8$  peptides and for positively charged  $(\text{KKK})_8$  and  $(\text{QKQ})_8$  peptides. The orange dotted line marks the gel-buffer interface. (E) and (F) show representative images of  $(\text{EEE})_8$  and  $(\text{KKK})_8$  peptides microinjected into the mouse cremaster muscle 5 min and 60 min post-injection. The negatively charged  $(\text{EEE})_8$  peptides rapidly leave the site of injection (white crosses, E) whereas the positively charged  $(\text{KKK})_8$  show increased intensity around the blood vessel and at the microinjection site (white crosses, F). Scale bar:  $50 \mu\text{m}$ .



Next, we ask if this charge-selective accumulation also occurs for smaller molecules. To answer this question, we compare the penetration profiles of the 150 kDa DEAE- or CM-dextran to variants of those molecules with a molecular weight of only 4 kDa. The smaller size of the 4 kDa dextrans will result in a higher diffusion coefficient in water. Thus, within the fixed duration of our experiments, we expect the smaller dextrans to enter more deeply into the channel than the 150 kDa dextrans. Indeed, after a time span of 60 min the 4 kDa dextrans diffuse further into the channel than their 150 kDa counterparts (see the dashed lines in Fig. 2C). Furthermore, we observe that also the positively charged 4 kDa dextrans accumulate at the interface whereas negatively charged dextrans do not. Also, the height of the accumulation peak seems to be similar for both DEAE-dextran variants.

### 150 kDa DEAE-dextrans accumulate around blood vessels in murine tissue

Of course, in our microfluidic assay many simplifications had to be introduced compared to the *in vivo* situation we aim to mimic. Thus, we next test whether a similar charge-dependent accumulation of dextrans also occurs in living tissue. For this purpose, we perform experiments in living mice and deposit differently sized and charged FITC-labeled dextrans into the mouse cremaster muscle by microinjection. As injection sites, we choose locations in close proximity to blood vessels (*i.e.* postcapillary venules). The venular basement membrane maintains the integrity of the blood vessel and, due to the dense network of matrix proteins, it constitutes a barrier for diffusing macromolecules and emigrating leukocytes.<sup>28</sup>

First, the distribution of injected 150 kDa DEAE-dextrans is investigated. From our *in vitro* experiments, we expect that those dextrans accumulate at the basolateral side of blood vessels where endothelial cells secrete basal lamina components. Indeed, within 5 min after microinjection (Fig. S3†) we observe a pronounced accumulation of 150 kDa DEAE-dextrans around nearby blood vessels, and this accumulation remains stable during the whole observation time of 60 min (Fig. 2E, white arrows). If this accumulation is also charge selective *in vivo*, then the CM-dextrans should exhibit a different behavior. Indeed, in contrast to the DEAE-dextrans, the CM-dextrans do not accumulate around blood vessels within the observation time of 60 min (Fig. 2D). They do, however, seem to concentrate in muscle fibers close to the injection site. We assume that, if the muscle is pierced by the glass capillary during microinjection, a fraction of the 150 kDa CM-dextrans is brought in direct contact with this muscle fiber and remains trapped there. For the 4 kDa dextran variants, this charge selective accumulation behavior is not as pronounced *in vivo* as it was in our *in vitro* setup (Fig. S4†).

### The net charge of a molecule sets its accumulation propensity

It was suggested previously that the surface properties of diffusing particles and molecules, *e.g.* their net charge, might

play a key role in determining their immobilization efficiency in extracellular matrices.<sup>14,29,30</sup> Polystyrene particles and liposomes trapped in the bulk volume of ECM gels possess a net charge of up to  $\pm 10^{10}e$  and  $\pm 10^5e$ , respectively. In contrast, the net charge is only +200e for the 150 kDa DEAE-dextrans and -165e for the 150 kDa CM-dextrans and +5e and -4e, respectively, for the 4 kDa dextran variants (Table 1). A direct comparison of nanoparticles and molecules is, of course, difficult. However, also comparing dextrans of different molecular weight is not trivial as those molecules carry different amounts of fluorophores in addition to their DEAE and CM functionalization.

To investigate the influence of the net charge of a molecule on its diffusion across ECM interfaces, we switch from dextran molecules to customized peptides. These synthetic peptides all have the same length, *i.e.* 24 amino acids, and carry one TAMRA label at the N-terminus. We compare the diffusion of four different amino acid sequences, which were designed to differ in terms of their net charge but have similar molecular weights: (KKK)<sub>8</sub> (high positive charge), (QQK)<sub>8</sub> (low positive charge), (EEE)<sub>8</sub> (high negative charge) and (QQE)<sub>8</sub> (low negative charge) (see Materials & methods for details). Representative images for the penetration profiles of (EEE)<sub>8</sub> and (KKK)<sub>8</sub> are shown in Fig. 3B and C.

Also with those peptides, we observe a clear difference between the behavior of positively charged molecules and their negatively charged counterparts at the gel/buffer interface (white arrows in Fig. 3C). In Fig. 3D, the penetration profiles are shown for the four different peptides 60 min after insertion through inlet 2 (see Fig. S5† for profiles after 5 min). The two negatively charged peptides, (EEE)<sub>8</sub> and (QQE)<sub>8</sub>, show a very similar behavior: they do not accumulate at the buffer-gel interface and their fluorescent intensity decreases as a function of the penetration depth as one would expect for diffusive transport according to Fick's law. (KKK)<sub>8</sub> and (QQK)<sub>8</sub> accumulate both at the gel/buffer interface, yet the intensity of this accumulation peak is higher for (KKK)<sub>8</sub> than for (QQK)<sub>8</sub>. However, the distribution profile of those peptides within the gel region is comparable to the negatively charged peptides. In contrast to the dextrans, the accumulation propensity of the two positively charged peptide variants can now directly be compared. We measure an accumulation peak intensity of 105% for (QQK)<sub>8</sub> and 133% for (KKK)<sub>8</sub>, respectively, compared to the fluorescent intensity of the peptides in the buffer compartment. It is reasonable to assume that the binding affinity of the strongly charged (KKK)<sub>8</sub> peptide to the ECM gel is larger than for the weakly charged (QQK)<sub>8</sub> peptide. Indeed, reducing the binding affinity in our model by an order of magnitude reproduces the decrease in the height of the accumulation peak observed in our *in vitro* experiments (Fig. 3A).

### Charged molecules accumulate at the basolateral side of blood vessel walls

To better specify which subsection of the tissue is responsible for the charge selective accumulation of molecules, we repeat



the microinjection with the different peptide variants and perform a colocalization test with key components from blood vessels. Already 5 min post-injection, negatively charged (EEE)<sub>8</sub> peptides spread from the injection site into the surrounding connective tissue and, after 60 min, a spatially homogeneous fluorescence signal is obtained (Fig. 3E). In contrast, when the (KKK)<sub>8</sub> peptide is injected into the muscle an accumulation around blood vessels is observed already 5 min post-injection (Fig. 3F, white arrows). At the end of our observation time, *i.e.* 60 min after injection, this locally increased intensity can still be detected around the blood vessel and is concentrated in perivascular (cellular) spots. Large parts of the positively charged (KKK)<sub>8</sub> peptides also remain at the injection site but no accumulation is observed in other areas of the connective tissue. This suggests that the peptides do not interact with collagen I, the main component of the connective tissue, which is supported by *in vitro* experiments conducted with collagen I gels (see Fig. S6†). Compared to the FITC-label of the dextrans, the TAMRA-label of the peptides exhibits a much higher photostability, which allows for an investigation of the (KKK)<sub>8</sub> peptide localization by means of immunohistochemical staining.

Consistent with the results obtained by microfluidics, (KKK)<sub>8</sub> peptides penetrate the connective tissue and accumulate around blood vessels. The evaluation of the images obtained by immunostaining shows that the accumulation sites of peptides colocalize with collagen IV fibers which constitute the basal lamina of blood vessels and thereby indicate the localization of the basal lamina (Fig. 4A–D). CD31 positive endothelial cells, lining the interior surface of blood vessels, do not colocalize with (KKK)<sub>8</sub> (Fig. 4E and H) which suggests that the peptides encounter a barrier that prevents them from reaching the inner volume of the blood vessel. Immunostaining with TO-PRO 3, a marker for cell nuclei, demonstrates a cellular uptake of peptides already 5 min after injection; however, internalization of peptides by endothelial cells is not observed (Fig. 4). Moreover, positively charged (KKK)<sub>8</sub> peptides exhibit a strong affinity for muscle

fibers (Fig. 4A and D) and unspecified fibrous components (Fig. 4E) of the interstitial space within the cremaster muscle. Immunostaining of samples obtained 60 min after microinjection (Fig. S7†) is consistent with the findings shown in Fig. 4.

## Conclusion

Here, we have introduced a microfluidic chip which allows for quantifying the diffusive transport of molecules across a liquid/ECM interface. The results obtained with this *in vitro* setup are in good agreement with *in vivo* experiments performed in the cremaster muscle of mice. Our findings suggest that the selective permeability properties of the extracellular matrix layer surrounding blood vessels contribute to regulating the diffusive entry of nanoparticles and molecules from the blood stream into the connective tissue or *vice versa*. In conclusion, for an even better approximation of complex biological barriers in a microfluidics setup, both the cellular monolayer as well as the adjoining biopolymer matrix should be incorporated into the chip. Such an approach might even open new avenues for creating predictive penetration tests that help us gaining a better understanding of highly complex biological interfaces such as the blood–brain-barrier.

## Experimental section

### Microfluidic channel

Soft lithography was used to fabricate the microfluidic chips. The channel geometry was designed using AutoCAD (Autodesk, Munich, Germany) and the mask was printed at a resolution of 64 000 dpi (Zitzmann, Eching, Germany). The master was fabricated on a silicon wafer (Siegert Wafer, Aachen, Germany) with EpoCore (micro resist technology, Berlin, Germany) as a negative photoresist. After spin coating (Laurell, North Wales, USA) onto the silicon wafer for 35 s at

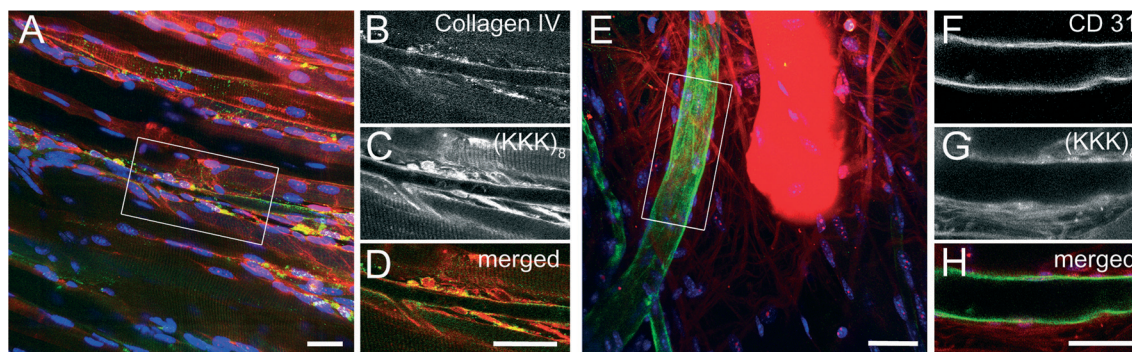


**Fig. 4** Confocal immunofluorescence images of (KKK)<sub>8</sub> peptides 5 min after microinjection into the murine cremaster muscle. 20 optical slices each were used to obtain a 3-dimensional rendering of blood vessels (A, E). A single confocal z-plane from the regions indicated in (A) and (E) are shown in (B–D) and (F–H). The tissue is immunostained for cell nuclei (TO-PRO3, blue), collagen IV (green; Fig. 4A, B and D) and endothelial cells (CD31; green; Fig. 4E, F and H). The (KKK)<sub>8</sub> peptide (red) strongly colocalizes with collagen IV at the basolateral side of endothelial cells of blood vessels. Scale bar: 30 μm.



1000 rpm two prebake steps were conducted: first at 65 °C for 5 min, second at 95 °C for 10 min. After cooling down, the photoresist was exposed to UV light for 7 min to ensure cross-linking. Post-exposure baking were conducted at 65 °C for 5 min and subsequently at 95 °C for 20 min. The wafer was developed using mr-Dev 600 (micro resist technology, Berlin, Germany) to remove all remaining uncrosslinked photoresist. Finally, the master was rinsed with isopropanol to remove remaining developer. For the microfluidic channel fabrication Sylgard 184 (Dow Corning, Midland, MI, USA) elastomer was mixed at a 10:1 ratio with curing agent, degassed for 30 min, poured onto the master and cured at 80 °C for 1 h. The cured PDMS was peeled off and bonded to a glass slide using oxygen plasma at 20 W for 30 s. The bonded device was stored in an oven at 120 °C overnight to regain its hydrophobic properties.

### ECM, dextrans and polypeptides

Growth factor reduced extracellular matrix gel (ECM) with a protein concentration of 7.37 mg mL<sup>-1</sup> purified from the Engelbreth-Holm-Swarm sarcoma of mice was obtained from Sigma-Aldrich. For experiments, ECM was thawed on ice for several hours and afterwards a volume of 2 µL was inserted into the microfluidic device through inlet 1. Fluorescein isothiocyanate-diethylaminoethyl (FITC-DEAE) and fluorescein isothiocyanate-carboxymethyl (FITC-CM) dextrans with an average molecular weight of 4 kDa and 150 kDa, respectively, was obtained from Sigma-Aldrich and dissolved in PBS at a concentration of 10 mg mL<sup>-1</sup>. Customized peptides were obtained from PEPperPRINT (Heidelberg, Germany) and used without further purification. The length of the customized peptides was chosen to match the molecular weight of the 4 kDa dextrans which leads to a peptide consisting of 24 amino acids. The diffusive transport of the peptides is evaluated by fluorescence microscopy, thus a carboxytetramethylrhodamine (TAMRA) label was conjugated to the N-termini of each peptide. In total, four different peptides were designed: a highly negatively charged, a highly positively charged, a moderate negatively charged, and a moderate positively charged peptide variant. The corresponding amino acid sequences are: TAMRA-(EEE)<sub>8</sub>, TAMRA-(KKK)<sub>8</sub>, TAMRA-(QQE)<sub>8</sub> and TAMRA-(QQK)<sub>8</sub>. Here, E represents glutamic acid, K denotes lysine and Q denotes glutamine (according to the 1-letter amino acid coding). Glutamic acid has a molecular weight of 147.13 g mol<sup>-1</sup>, and the free side-chain carboxylic acid group of this amino acid has a pK<sub>a</sub> of 4.1. This results in a negatively charged group at physiological pH which is used in our experiments. Lysine has a molecular weight of 146.19 g mol<sup>-1</sup>, and the pK<sub>a</sub> of the side chain amino group is 10.5; as a consequence, this amino acid is positively charged at neutral pH. Glutamine has a molecular weight of 146.15 g mol<sup>-1</sup> and a zwitterionic side chain. Glutamine therefore assumed to be net neutral at pH 7. For the experiments, the peptides were dissolved in PBS and used at a concentration of 1 mg mL<sup>-1</sup>.

Buffer containing test molecules was carefully inserted into inlet 2 with a Hamilton syringe (1702 sleeve type), which ejects a volume of 0.33 µL per rotation. When the channel was completely filled with buffer the flow was stopped to match the *in vivo* situation where the test molecules are injected into the connective tissue. Thus, after a short time of equilibration no flow of test molecules is present.

### Data acquisition and evaluation

Images were acquired with a digital camera (Orca Flash 4.0 C11440, Hamamatsu, Japan) using the software Hokawo provided by Hamamatsu on an AxioVert 200 (Zeiss, Oberkochen, Germany) microscope using a 4× objective (Zeiss, Oberkochen, Germany). The exposure time was chosen such that no pixel saturation occurred. Each of the six channels was analyzed individually with ImageJ. A rectangle with a height of 880 pixels corresponding to 2.75 mm and a width of 30 pixels (0.09 mm) was placed in the channel such that 50 (0.16 mm) pixels of this rectangle were located in the lower channel (Fig. 1B). This procedure allows us to account for the bleaching of the fluorescent label of the test molecules. Since no continuous flow was applied, the fluorophores in the buffer compartment are subjected to same rate of bleaching as the molecules within the ECM. Therefore, the fluorescence intensity in the buffer channel (calculated from the 50 pixels of the rectangle in the lower channel) was used as a reference to normalize the intensity in the finger-like structure. This ensures the comparability of the calculated intensity profiles at different time points during the experiments.

The intensity within the chosen rectangle was averaged per pixel line with a function implemented in ImageJ. Thus, one intensity value per line was obtained. In a next step, these average intensity values per line were averaged again, first over the six finger channels of a chip and then over three different microfluidic chips.

### Animals and surgical procedure

Male C57BL/6 mice at the age of 10–12 weeks were purchased from Charles River (Sulzfeld, Germany). Animals were housed under conventional conditions with free access to food and water. All experiments were performed according to German legislation for the protection of animals. The surgical preparation was performed as described by Baez<sup>31</sup> with minor modifications. Briefly, mice were anesthetized by intraperitoneal injection of a ketamine/xylazine mixture (100 mg kg<sup>-1</sup> ketamine and 10 mg kg<sup>-1</sup> xylazine). The right cremaster muscle was exposed through a ventral incision of the scrotum. The muscle was opened ventrally in a relatively avascular zone, using careful electrocautery to stop any bleeding, and spread over the pedestal of a custom-made microscopy stage. Epididymis and testicle were detached from the cremaster muscle and placed into the abdominal cavity. Throughout the procedure as well as after surgical preparation during *in vivo* microscopy, the muscle was superfused with warm



buffered saline. The body temperature was maintained at 37 °C using a heating pad placed under the mouse. After *in vivo* microscopy, tissue samples of the cremaster muscle were prepared for immunohistochemistry. Anaesthetized animals were then euthanized by an intra-arterial pentobarbital overdose (Narcoren, Merial, Hallbergmoos, Germany).

### *In vivo* microscopy

The setup for *in vivo* microscopy was centered around an VisiScope.A1 imaging system (Visitron Systems GmbH, Puchheim, Germany), equipped with a LED light source for fluorescence epi-illumination. For excitation of dextrans the 470 nm, for the excitation of peptides the 550 nm LED modules (exposure time 100 ms), and for transillumination the 655 nm LED module (exposure time 10 ms) were used in a fast simultaneous mode. Light was directed onto the specimen *via* a triple dichroic filter NC316973 (z 405/488/561 rpc; Chroma Technology Corp., Bellows Falls, VT, USA). Images were obtained with a water dipping objective (20×, NA 1.0). Light from the specimen was separated with a beam splitter (T 580 lpxr Chroma Technology Corp., Bellows Falls, VT, USA) and acquired with two Rolera EM2 cameras and VisiView Imaging software (Visitron).

### Microinjection of dextran and peptides

Local administration of 250 ± 100 pL of fluorescently labeled dextran (2 mg mL<sup>-1</sup>) or peptides (1 mg mL<sup>-1</sup>) into the cremaster muscle was performed *via* perivenular microinjection in regions at a distance of 25 to 50 μm from a postcapillary venule.<sup>32</sup> Venules with diameters ranging between 25 and 35 μm were selected for the experiments. Microinjection was performed under visual control of the intravital microscope, with a long distance air objective (20×, NA 0.4 Olympus), using borosilicate glass micropipettes (GB150TF-8P, Science Products GmbH, Hofheim, Germany) – pulled with a micropipette puller (PC 10, Narishige, London, United Kingdom) – which were connected to the injection system consisting of a micromanipulator (PatchStar Micromanipulator, Scientifica, Uckfield, United Kingdom) and a microinjector (FemtoJet, Eppendorf, Hamburg, Germany). The tip pressure during injection was 3000 hPa and the tip diameter <1 μm. The vessel and the surrounding tissue were visualized during a time period from 1 min to 60 min after injection.

Mice ( $n = 3$  each group) received 150 kDa CM-dextran, 150 kDa DEAE-dextran, (KKK)<sub>8</sub> peptides and (EEE)<sub>8</sub> peptides *via* microinjection 20 min after the preparation of the cremaster muscle. The animals were randomly assigned to the experimental groups.

### Immunostaining

To determine the charge dependent localization of peptides, immunostaining of the cremaster muscle was performed. After dissection, the tissue was fixed with 2% paraformaldehyde for 15 min at room temperature, then blocked and

permeabilized in PBS, supplemented with 2% bovine serum albumin (Sigma Aldrich, Munich, Germany) and 0.5% Triton X-100 (Sigma Aldrich, Munich, Germany) for 1 h at room temperature. After incubation with a rabbit polyclonal Collagen IV antibody (ab6586, Abcam, Cambridge, UK) or rat anti mouse CD31 (Clone MEC 13.3, 553 370, BD Pharmingen, Heidelberg, Germany) at room temperature for 2 h, the tissues were washed with PBS and incubated with an Alexa-Fluor 488-linked goat anti-rabbit or Alexa-Fluor 488-linked goat anti-rat antibody (Life Technologies, Darmstadt, Germany) and TO-PRO3@-Iodide (Invitrogen, Carlsbad, CA, USA) for another 2 h at room temperature in the dark. Immunostained cremaster muscles were mounted in PermaFluor (Beckman Coulter, Krefeld, Germany) on glass slides. Images were obtained using a Leica SP5 confocal laser-scanning microscope, equipped with a GaAsP hybrid detection system (Leica HyD), with an oil-immersion lens (63×; NA 1.40; Leica Microsystems, Wetzlar, Germany). Images were processed with ImageJ software and figures for publication were assembled in Photoshop 9 (Adobe Systems, Mountain View, California, US).

### Numerical simulations

For the simulation of molecular penetration across an ECM gel, we used a standard diffusion–reaction model in one dimension that includes the binding and unbinding processes to the gel (see ESI† for a detailed description). Two coupled partial differential equations were numerically solved by discretizing space and time. The solution was propagated stepwise in time by an Euler-forward scheme, with a fixed time step chosen to ensure numerical stability.

### Funding sources

This work was supported by the Deutsche Forschungsgemeinschaft through project B7 “Nanoagents in 3-dimensional biopolymer hydrogels”, project B10 “Spatio-temporal control of immune cell trafficking by multifunctional nanoconstructs *in vivo*” and project A3 “Spatially orchestrated stochastic enzyme kinetics in multi-enzyme complexes” in the framework of SFB 1032.

### References

- 1 K. Y. Tsang, M. C. Cheung, D. Chan and K. S. Cheah, The developmental roles of the extracellular matrix: beyond structure to regulation, *Cell Tissue Res.*, 2010, **339**, 93–110.
- 2 S. M. Gabe, Gut barrier function and bacterial translocation in humans, *Clin. Nutr.*, 2001, **20**, 107–112.
- 3 O. Lieleg and K. Ribbeck, Biological hydrogels as selective diffusion barriers, *Trends Cell Biol.*, 2011, **21**, 543–551.
- 4 R. Cecchelli, V. Berezowski, S. Lundquist, M. Culot and M. Renftel, *et al.*, Modelling of the blood–brain barrier in drug discovery and development, *Nat. Rev. Drug Discovery*, 2007, **6**, 650–661.
- 5 E. Proksch, J. M. Brandner and J. M. Jensen, The skin: an indispensable barrier, *Exp. Dermatol.*, 2008, **17**, 1063–1072.





- 6 M. A. McGuckin, S. K. Linden, P. Sutton and T. H. Florin, Mucin dynamics and enteric pathogens, *Nat. Rev. Microbiol.*, 2011, **9**, 265–278.
- 7 B. J. Teubl, M. Absenger, E. Frohlich, G. Leitinger and A. Zimmer, *et al.*, The oral cavity as a biological barrier system: Design of an advanced buccal *in vitro* permeability model, *Eur. J. Pharm. Biopharm.*, 2013, **84**, 386–393.
- 8 A. M. Alkilany, A. Shatanawi, T. Kurtz, R. B. Caldwell and R. W. Caldwell, Toxicity and Cellular Uptake of Gold Nanorods in Vascular Endothelium and Smooth Muscles of Isolated Rat Blood Vessel: Importance of Surface Modification, *Small*, 2012, **8**, 1270–1278.
- 9 J. R. Turner, Intestinal mucosal barrier function in health and disease, *Nat. Rev. Immunol.*, 2009, **9**, 799–809.
- 10 K. Maruyama, O. Ishida, T. Takizawa and K. Moribe, Possibility of active targeting to tumor tissues with liposomes, *Adv. Drug Delivery Rev.*, 1999, **40**, 89–102.
- 11 S. K. Hobbs, W. L. Monsky, F. Yuan, W. G. Roberts and L. Griffith, *et al.*, Regulation of transport pathways in tumor vessels: Role of tumor type and microenvironment, *Proc. Natl. Acad. Sci. U. S. A.*, 1998, **95**, 4607–4612.
- 12 M. Simionescu, D. Popov and A. Sima, Endothelial transcytosis in health and disease, *Cell Tissue Res.*, 2009, **335**, 27–40.
- 13 T. M. Allen and P. R. Cullis, Drug delivery systems: Entering the mainstream, *Science*, 2004, **303**, 1818–1822.
- 14 O. Lieleg, R. M. Baumgärtel and A. R. Bausch, Selective Filtering of Particles by the Extracellular Matrix: An Electrostatic Bandpass, *Biophys. J.*, 2009, **97**, 1569–1577.
- 15 F. Arends, R. Baumgartel and O. Lieleg, Ion-specific effects modulate the diffusive mobility of colloids in an extracellular matrix gel, *Langmuir*, 2013, **29**, 15965–15973.
- 16 W. H. De Jong and P. J. A. Borm, Drug delivery and nanoparticles: Applications and hazards, *Int. J. Nanomed.*, 2008, **3**, 133–149.
- 17 L. G. Griffith and M. A. Swartz, Capturing complex 3D tissue physiology *in vitro*, *Nat. Rev. Mol. Cell Biol.*, 2006, **7**, 211–224.
- 18 E. Esch, A. Bahinski and D. Huh, Organs-on-chips at the frontiers of drug discovery, *Nat. Rev. Drug Discovery*, 2015, **14**, 248–260.
- 19 K. Ziolkowska, R. Kwapiszewski and Z. Brzozka, Microfluidic devices as tools for mimicking the *in vivo* environment, *New J. Chem.*, 2011, **35**, 979–990.
- 20 Z. Ma, S. Koo, M. A. Finnegan, P. Loskill and N. Huebsch, *et al.*, Three-dimensional filamentous human diseased cardiac tissue model, *Biomaterials*, 2014, **35**, 1367–1377.
- 21 Y. Kim, M. E. Lobatto, T. Kawahara, B. L. Chung and A. J. Mieszawska, *et al.*, Probing nanoparticle translocation across the permeable endothelium in experimental atherosclerosis, *Proc. Natl. Acad. Sci. U. S. A.*, 2014, **111**, 1078–1083.
- 22 D. Huh, B. D. Matthews, A. Mammoto, M. Montoya-Zavala and H. Y. Hsin, *et al.*, Reconstituting Organ-Level Lung Functions on a Chip, *Science*, 2010, **328**, 1662–1668.
- 23 L. Li, O. Lieleg, S. Jang, K. Ribbeck and J. Han, A microfluidic *in vitro* system for the quantitative study of the stomach mucus barrier function, *Lab Chip*, 2012, **12**, 4071–4079.
- 24 L. D. Li, T. Crouzier, A. Sarkar, L. Dunphy and J. Han, *et al.*, Spatial Configuration and Composition of Charge Modulates Transport into a Mucin Hydrogel Barrier, *Biophys. J.*, 2013, **105**, 1357–1365.
- 25 F. Arends, C. Nowald, K. Pflieger, K. Boettcher, S. Zahler and O. Lieleg, The Biophysical Properties of Basal Lamina Gels Depend on the Biochemical Composition of the Gel, *PLoS One*, 2015, **10**(2), e0118090.
- 26 C. J. Dowd, C. L. Cooney and M. A. Nugent, Heparan sulfate mediates bFGF transport through basement membrane by diffusion with rapid reversible binding, *J. Biol. Chem.*, 1999, **274**, 5236–5244.
- 27 E. G. Atkinson, S. Jones, B. A. Ellis, D. C. Dumonde and E. Graham, Molecular size of retinal vascular leakage determined by FITC-dextran angiography in patients with posterior uveitis, *Eye*, 1991, **5**(Pt 4), 440–446.
- 28 M. B. Voisin, D. Probstl and S. Nourshargh, Venular Basement Membranes Ubiquitously Express Matrix Protein Low-Expression Regions Characterization in Multiple Tissues and Remodeling during Inflammation, *Am. J. Pathol.*, 2010, **176**, 482–495.
- 29 R. G. Thorne, A. Lakkaraju, E. Rodriguez-Boulan and C. Nicholson, In vivo diffusion of lactoferrin in brain extracellular space is regulated by interactions with heparan sulfate, *Proc. Natl. Acad. Sci. U. S. A.*, 2008, **105**, 8416–8421.
- 30 S. Lelu, S. P. Strand, J. Steine and C. D. Davies, Effect of PEGylation on the Diffusion and Stability of Chitosan-DNA Polyplexes in Collagen Gels, *Biomacromolecules*, 2011, **12**, 3656–3665.
- 31 S. Baez, Open Cremaster Muscle Preparation for Study of Blood-Vessels by *in-vivo* Microscopy, *Microvasc. Res.*, 1973, **5**, 384–394.
- 32 S. Sellner, S. Kocabey, K. Nekolla, F. Krombach and T. Liedl, *et al.*, DNA nanotubes as intracellular delivery vehicles *in vivo*, *Biomaterials*, 2015, **53**, 453–463.

